AFRL-RX-WP-TR-2013-0202

INTEGRATED PHOTONIC CIRCUIT FABRICATION FOR ENABLING RF EMITTER ARRAY

F. Kenneth Hopkins

AFRL/RXAP

Kevin M. Walsh and Alexander Benken

University of Louisville

SEPTEMBER 2013
Interim Report

STINFO COPY

AIR FORCE RESEARCH LABORATORY
MATERIALS AND MANUFACTURING DIRECTORATE
WRIGHT-PATTERSON AIR FORCE BASE, OH 45433-7750
AIR FORCE MATERIEL COMMAND
UNITED STATES AIR FORCE

NOTICE AND SIGNATURE PAGE

Qualified requestors may obtain copies of this report from the Defense Technical Information Center (DTIC) (http://www.dtic.mil)

AFRL-RX-WP-TR-2013-0202 HAS BEEN REVIEWED AND IS APPROVED FOR PUBLICATION IN ACCORDANCE WITH ASSIGNED DISTRIBUTION STATEMENT.

_____//SIGNED//_____   _____//SIGNED//_____
ROBERT L. NELSON, Program Manager   DANIEL J. BREWER, Chief
Photonic Materials Branch   Photonic Materials Branch
                                        Functional Materials Division

_____//SIGNED//_____
KAREN R. OLSON, Deputy Chief
Functional Materials Division
Materials & Manufacturing Directorate

REPORT DOCUMENTATION PAGE

1. REPORT DATE *(DD-MM-YY)*	2. REPORT TYPE	3. DATES COVERED *(From - To)*
September 2013	Interim	27 August 2012 – 31 August 2013

4. TITLE AND SUBTITLE
INTEGRATED PHOTONIC CIRCUIT FABRICATION FOR ENABLING RF EMITTER ARRAY

5a. CONTRACT NUMBER
In-House

5b. GRANT NUMBER

5c. PROGRAM ELEMENT NUMBER
62102F

6. AUTHOR(S)
F. Kenneth Hopkins (AFRL/RXAP)
Kevin M. Walsh and Alexander Benken (University of Louisville)

5d. PROJECT NUMBER
4347

5e. TASK NUMBER

5f. WORK UNIT NUMBER
X09B (PS114100)

7. PERFORMING ORGANIZATION NAME(S) AND ADDRESS(ES)

AFRL/RXAP
3005 Hobson Way
Wright-Patterson AFB, OH 45433

University of Louisville
Electrical & Computer Engineering
Louisville, KY 40292

8. PERFORMING ORGANIZATION REPORT NUMBER

9. SPONSORING/MONITORING AGENCY NAME(S) AND ADDRESS(ES)
Air Force Research Laboratory
Materials and Manufacturing Directorate
Wright-Patterson Air Force Base, OH 45433-7750
Air Force Materiel Command
United States Air Force

10. SPONSORING/MONITORING AGENCY ACRONYM(S)
AFRL/RXAP

11. SPONSORING/MONITORING AGENCY REPORT NUMBER(S)
AFRL-RX-WP-TR-2013-0202

12. DISTRIBUTION/AVAILABILITY STATEMENT
Approved for public release; distribution is unlimited.

13. SUPPLEMENTARY NOTES
Approved by 88ABW Public Affairs Office: Case number 88ABW-2013-4657 on 06-Nov-13. Report contains color.

14. ABSTRACT

The interim report describes an initial effort to fabricate an Integrated Photonic Circuit (IPC) which provides a means for converting an optical laser signal, that consists of both a narrow-line carrier wavelength and a heterodyned RF signal that are in-phase, to an electrical RF signal that can drive various on-chip components such as an antenna. The IPC would supply a critical missing element for enabling new phased-array radar based on an all-optical architecture. Ge-on-Si technology, the focus of the effort, has specific advantages that are fundamental to nearly all integrated photonic circuits. Its direct energy bandgap, slightly larger than Ge's indirect bandgap, permits band-to-band recombination/generation at an energy that corresponds to light near the standard optical communications wavelength. Ge-on-Si technology, therefore, could enable a host of IPC subcomponents including photodetectors, laser diodes, and enhanced silicon modulators. In addition, such germanium devices can be simply and inexpensively incorporated into a silicon manufacturing process.

15. SUBJECT TERMS
integrated photonics, germanium, photodetector, heterodyne detector

16. SECURITY CLASSIFICATION OF:			17. LIMITATION OF ABSTRACT:	18. NUMBER OF PAGES	19a. NAME OF RESPONSIBLE PERSON (Monitor)
a. REPORT	**b. ABSTRACT**	**c. THIS PAGE**	SAR	23	Robert L. Nelson
Unclassified	Unclassified	Unclassified			19b. TELEPHONE NUMBER *(Include Area Code)* (937) 255-9904

TABLE OF CONTENTS

LIST OF FIGURES

LIST OF TABLES

1.0 INTRODUCTION

During the 1990's, many radar experts understood that very large phased-array radar on either aircraft or space platforms could only be realized with photonic control utilizing high bandwidth optical fiber, electro-optic (EO) modulators, and optical detectors. The approach promised significant savings in the radar system's size, weight, and power as compared with all-electronic approaches. This early photonic development effort utilized amplitude modulation to encode information on a laser carrier, and unfortunately, the linear dynamic range of an electro-optic modulator is extremely limited. In other words, the approach was not feasible. Yet, the effort served to encourage the development of new materials that are now proving to be transformational.

A new photonic approach was recently proposed that utilizes phase modulation versus amplitude modulation. [1] It utilizes (a) polarized single mode fiber, (b) EO modulators for wavelength mixing of optical and electronic signals ($\omega_2 = \omega_C + \omega_{RF}$) for which the carrier frequency (ω_C) is coherently phase-locked to the sideband frequency (ω_2), and (c) photodetectors for heterodyne detection (for a photodiode, current =DC component + ω_{RF} component). A schematic of the basic approach is illustrated in Figure 1, showing the control of two pixels of a phased-array emitter.

The technical objective of the research described in this report is to investigate materials and materials structures to enable an integrated photonic circuit optical heterodyne detection for driving an antenna element of a phased array. Two approaches were considered to enable a compact and efficient heterodyne detector that is coupled to an antenna, heterodyne detection utilizing either a second-order nonlinear optical waveguide or a photodetector.

Two precepts should be recognized regarding integrated photonic circuits. First, IPCs require a common substrate, for which silicon has recognized advantages. Commercially available silicon wafers are large, inexpensive, offer extreme flatness for optical components, excellent electronic properties for integration with electronic devices, compatibility with many epitaxial materials, and potential for simple integration with optical fiber using v-groove fabrication. Second, IPC operation at a 1.55 µm wavelength has advantages for compatibility with optical communications systems and subcomponents already developed for the optical communications industry.
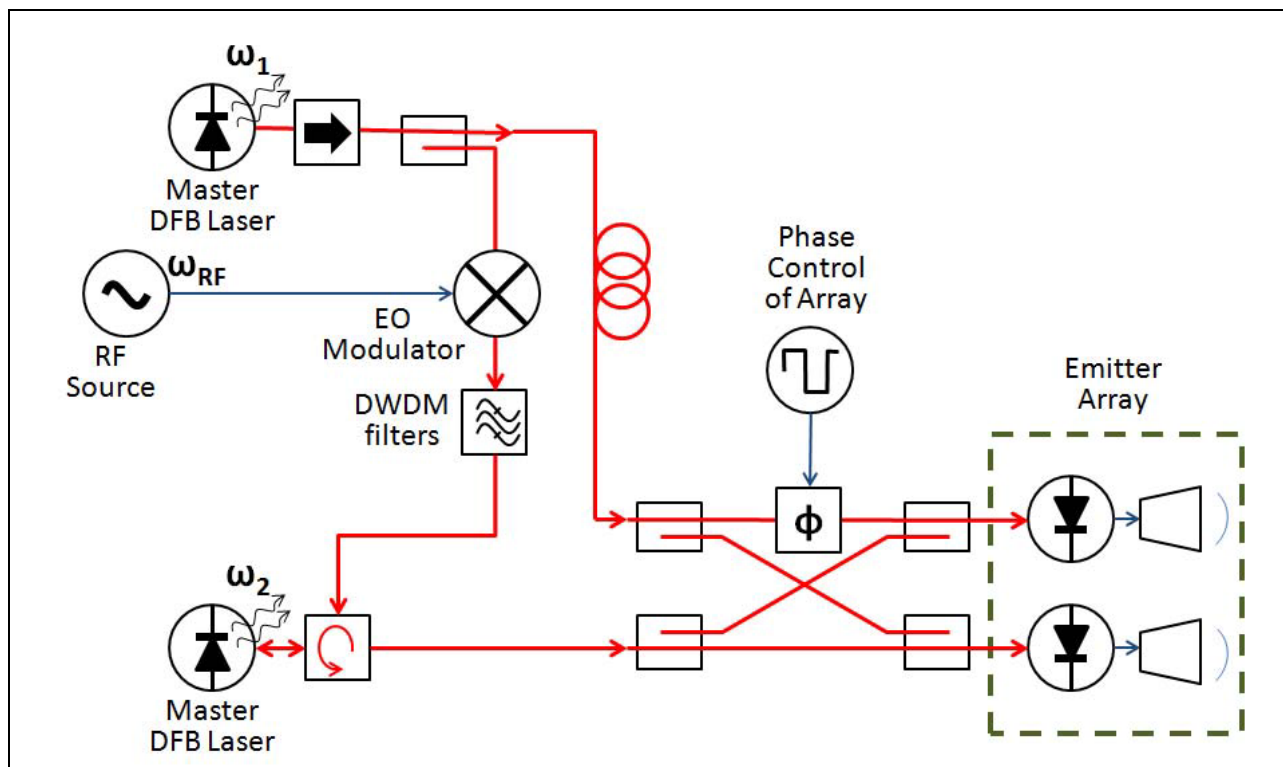
Figure 1: Photonic approach to RF phased-array

Approved for public release; distribution unlimited

2.0 APPROACHES

Optical heterodyne detection refers to the conversion of laser light made up of an optical or carrier frequency (ω_C) that is modulated at frequency (ω_{RF}) and to an electrical signal at ω_{RF} for driving electronic components. In this case, the component is a micro-antenna, an element of a phased array antenna, and possibly associated electronics that interface the heterodyne detector to the antenna. Two approaches to heterodyne detection were compared under the task. The first approach utilizes a nonlinear optical waveguide, and the second uses a photodetector.

2.1 Nonlinear Optical Waveguide

In the first approach, a second-order nonlinear-optical polymer waveguide is utilized for converting the modulated optical signal to a voltage to drive the antenna element. The waveguide concentrates the laser light for efficient generation of a ω_{RF} term that appears as a voltage across the waveguide. If electrodes are placed across this region of the waveguide, then the electrodes can be directly connected to the antenna element or its associated electronic components.

The conversion of the modulated optical signal to the RF electrical signal is easily derived. Assume that the electric field E of the optical signal is composed of two components, E_1 at frequency ω_c and E_2 at ω_{RF}. The electric polarization (P) across the guide is then:

$$P \cong \varepsilon_o(\chi E + \chi_2 E^2)$$
$$= \varepsilon_o \chi[E_1 \cos \omega_c t + E_2 \cos(\omega_c + \omega_{RF})t] + \varepsilon_o \chi_2[E_1 \cos \omega_c t + E_2 \cos(\omega_c + \omega_{RF})t]^2$$
$$= \varepsilon_o \chi_1[E_1 \cos \omega_c t + E_2 \cos(\omega_c + \omega_{RF})t]$$
$$+ \varepsilon_o \chi_2 \{E_1^2(\frac{1}{2} + \frac{1}{2}\cos 2\omega_c t) + E_2^2[\frac{1}{2} + \frac{1}{2}\cos 2(\omega_c + \omega_{RF})t] + E_1 E_2[\cos \omega_{RF} t + \cos(2\omega_c + \omega_{RF})t]\} \qquad (1)$$

It is assumed in equation (1) that higher order nonlinear susceptibilities for the material beyond χ_2 are negligible, and ε_o is the permittivity of free space. The expression clearly shows that the nonlinear optical waveguide generates a ω_{RF} term.

The approach was proposed in 1998 and fully demonstrated in 2005. [2,3] There are a number of advantages and disadvantages to this as compared with a photovoltaic detector approach, one advantage being RF frequency responses to 400 GHz. [4] Yet, potential responsivities are unreasonably low, on the order of 9 mA/W for optimal performance. [4] The extremely low potential performance is sufficient justification to not further investigate this approach.

2.2 Photodetector

In the second approach, a photodetector such as a photodiode operating in the photovoltaic regime detects the laser light. The resulting signal either directly or indirectly drives the antenna element of a phased array. If the photodiode is biased such that the voltage across the junction is less than the thermal voltage, kT/q, the current from the photodiode is given by

Approved for public release; distribution unlimited

$$I_{diode} = I_{darkcurrent} + I_{photocurrent}$$

$$\cong C[\exp(\frac{qV}{mkT}) - 1] - q\eta AQ_s$$

$$\cong C[\exp(\frac{qV}{kT}) - 1] - \frac{q\eta\lambda\varepsilon_o A}{4\pi\hbar}E^2 \qquad (2)$$

where the dark current is assumed to be dominated by the bulk diffusion current, where Q_S is the photon flux of the laser light entering the depletion region of the photodiode, and where the electric field associated with the laser light is E. In addition, q is the charge on an electron, λ is the wavelength of light, ε_o is the permittivity of free space, A is the area of the detector, and $\hbar$ is Planck's constant over 2π. The E^2 expression in equation (2) can be expanded in the following manner to show how the ω_{RF} term is generated.

$$E^2 = [E_1\cos\{\omega_c t\} + E_2\cos\{(\omega_c + \omega_{RF})t\}]^2$$

$$= \frac{E_1^2}{2} + \frac{E_2^2}{2} + \frac{E_1^2}{2}\cos\{2\omega_c t\} + \frac{E_2^2}{2}\cos\{2(\omega_c + \omega_{RF})t\} + \frac{E_1 E_2}{4}\cos\{(2\omega_c + \omega_{RF})t\} + \frac{E_1 E_2}{4}\cos\{\omega_{RF}t\} \qquad (3)$$

Again, the expression clearly shows that the detector generates an ω_{RF} term.

High-performance 1.55 µm photodetectors, compatible with silicon substrates, do not presently exist. Silicon photodiodes' extrinsic detection of 1.55µm light is quite inefficient and slow (<1GHz). Photodiodes based on indium gallium arsenide are fast, well developed, and highly responsive to 1.55 µm light but have limited potential for true integration with silicon and optical waveguides. In contrast, germanium photodiodes have demonstrated high responsivity and fast speed with the added benefit of true integration. [5,6] The detectors' responsivities for gallium indium arsenide versus germanium are contrasted in Figure 2.
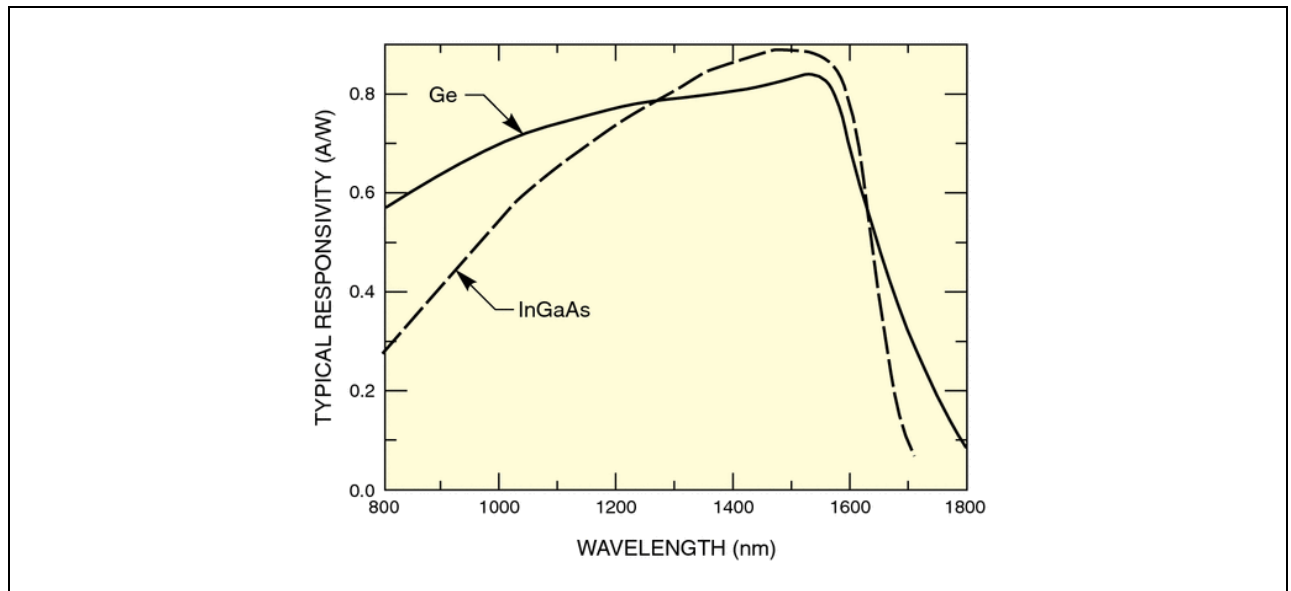

Figure 2: Typical responsivity of Ge and InGaAs photodiodes

A phototransistor structure is possibly a more relevant photodetector for integrated photonics than a photodiode as shown in Figure 3. The p-type germanium layer serves as the transistor's base, and its thickness is much less than Ge's minority electron diffusion length. The phototransistor should provide better characteristics for driving additional on-chip electronic and optical components by operating the device in the active region with a forward biased emitter-base junction and a reverse biased collector-base junction. The silicon optical waveguide that directs the optical modulated signal to the phototransistor has a bottom silica cladding layer that is tapered to a germanium layer in order to minimize light scattering at the waveguide-detector interface.
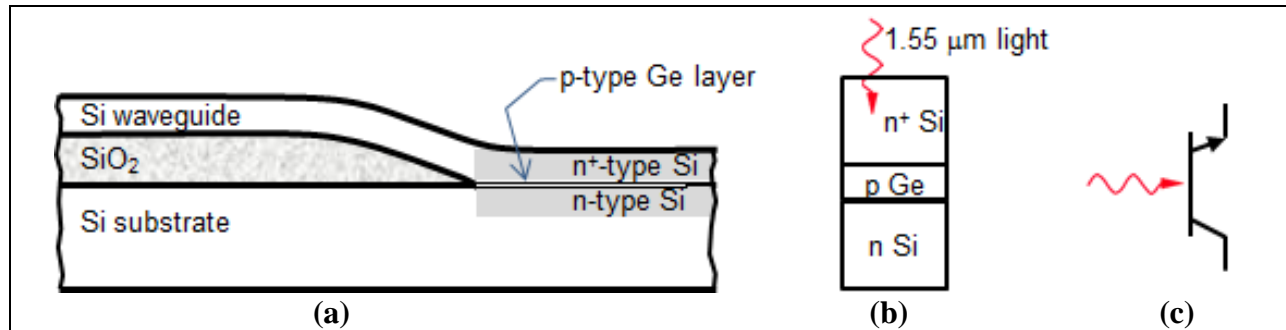

Figure 3: (a) Physical layout of a Ge phototransistor, (b) cross-section of the transistor, and (c) the associated circuit symbol

3.0 COMPONENT DESIGN

The designs for two components of the integrated photonic circuit were explored under the task. The optical fiber mount and the photodiode are the most obvious subcomponents to integrate and possibly the most challenging.

3.1 Optical Fiber Mount

A v-groove is a commonly utilized approach for aligning an optical fiber to a photodetector that could be combined using architecture similar to that illustrated in Figure 4.
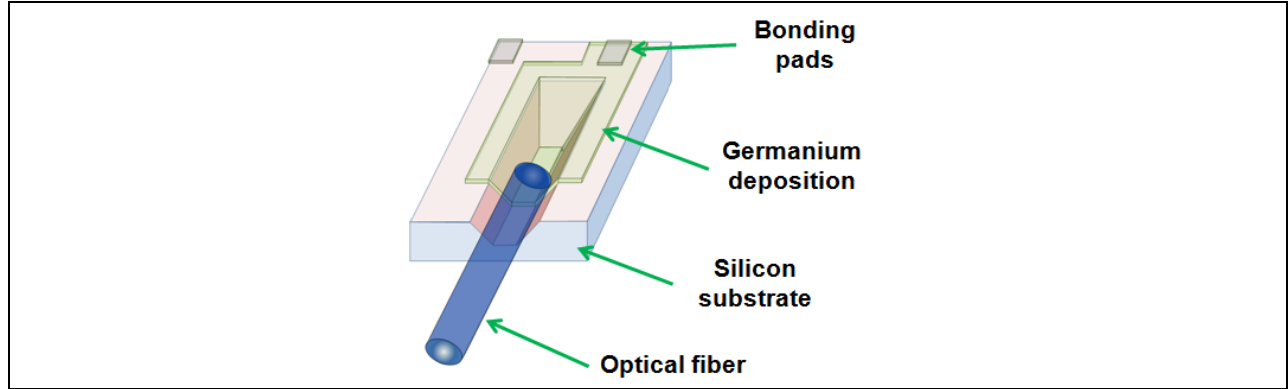
Figure 4 Potential architecture for v-groove/photodetector integration

What are the geometry and dimensions of the v-groove that would be required to be etched into the silicon substrate? Consider Figure 5 which illustrates a fiber in a v-groove for which r is the radius of the fiber and ϕ is the angle (ϕ=54.74°) between the (100) and (111) Si lattice planes. The v-groove width (w) can be related to these constants by the following derivation. From Figure 5, the depth of the v-groove is

$$d = 2r + x \qquad (4)$$

In addition, the following two expressions can be written for the two triangles drawn in Figure 5b:

$$tan\emptyset = \frac{d}{w/2} = \frac{2r + x}{w/2} \qquad (5)$$

$$cos\emptyset = \frac{r}{r + x} \qquad (6)$$

Approved for public release; distribution unlimited

Figure 5: V-groove / fiber geometry

Combining these equations and solving for w, the following results:

$$w = 2r(\cot\emptyset + \csc\emptyset) \tag{7}$$
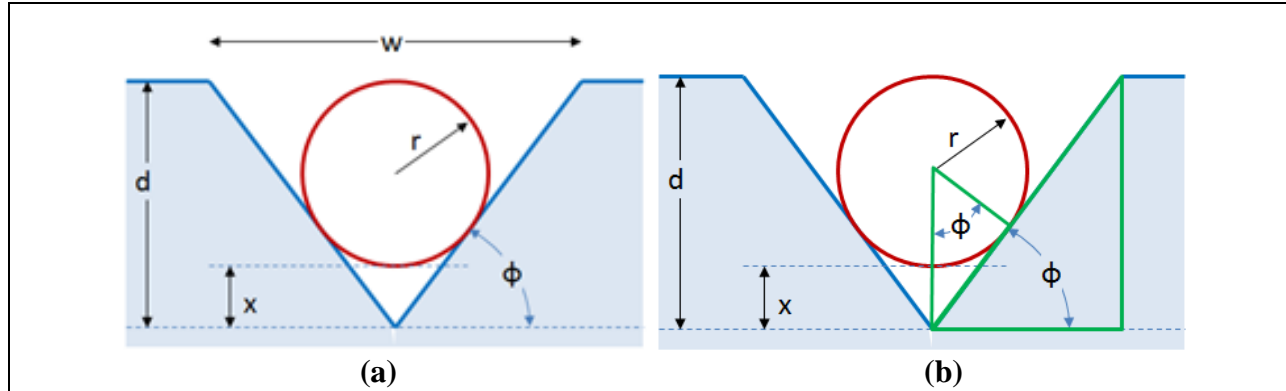
The radius of the fiber was obtained by contacting the company, Phase Sensitive Innovations, Inc. of Newark, DE. The company is presently helping AFRL to demonstrate the photonic-controlled RF emitter system for which the present task could enable a potential component. Dr. Christopher Schuetz of Phase Sensitive Innovations is using a standard phase-maintaining Panda optical fiber (see Figure 6) for the demonstration. It is available from Thorlabs (item # PM1550-HP). The outer diameter of the fiber is 125 ± 1 µm.
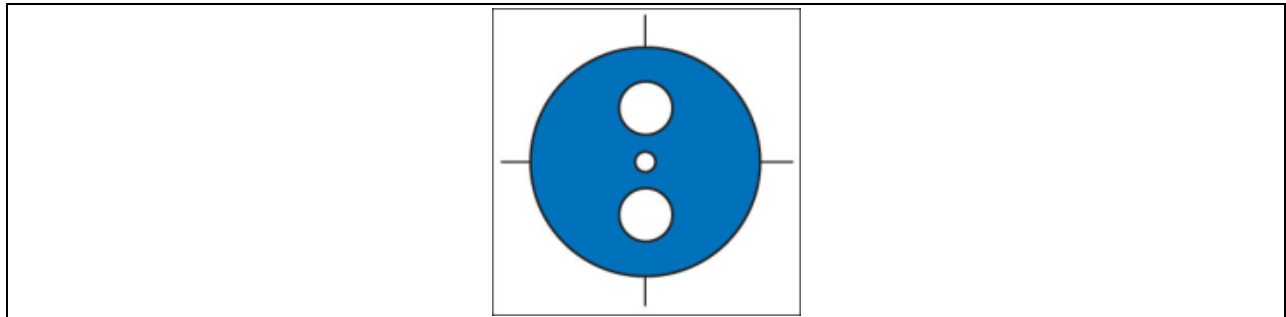
Figure 6: Panda style optical fiber

Using the maximum diameter of the fiber (126 µm) in the equation above, the v-groove width is calculated to be 241.5 µm. In addition, the etch depth could range from 2r (126 µm) to 2r+x (171 µm). A value of 130 µm is perhaps an ideal target for the etch depth. For v-groove fabrication using a KOH etchant at 85°C, the silicon etch time would then be (130 µm)/(1.4µm/min) = 93 minutes.

3.2 Photodetector

The initial design of a Ge-on-Si photodiode under this task entails the deposition of a few nanometer thick Ge layer on a Si (100) n-type substrate followed by a shallow phosphorous implantation extending into the silicon, activation annealing, and thick Ge growth. Defects in the thick Ge film provide effective p-type doping. [7] This test photodiode structure is illustrated in Figure 7.

Approved for public release; distribution unlimited

Figure 7: (a) Physical layout of a Ge photodiode, (b) cross-section of the detector region, and (c) the associated energy band diagram
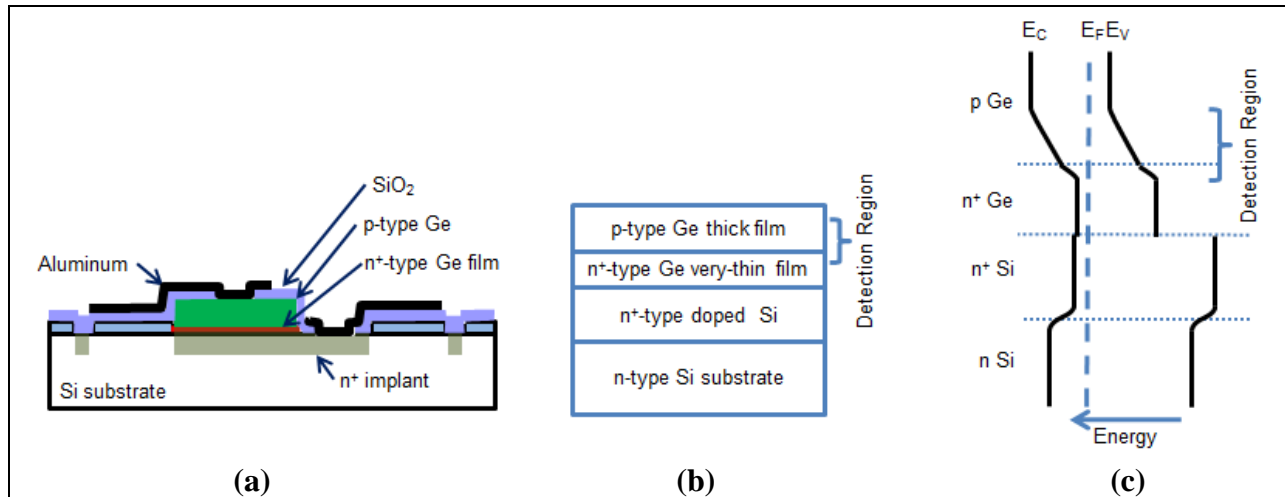
The design of a Ge-on-Si photodiode is complicated by the energy band mismatch at the Si-Ge junction. For the specific photodiode shown in Figure 7, the Si–Ge junction is ohmic since electrical conduction in the n^+ regions of the two sides of the junction is due to conduction-band electrons, the majority charge carriers, and since the conduction band in the vicinity of the junction is relatively smooth. In contrast, the junction blocks the movement of valence-band holes moving from the Ge to the Si, but the effect on electrical characteristics is negligible because these are minority carriers. It should be noted, however, that careless choice of doping such as a p-type Ge film on a n-type Si substrate will result in a rectifying contact as illustrated in Figure 8 for one of the Si-Ge junctions fabricated under this task.
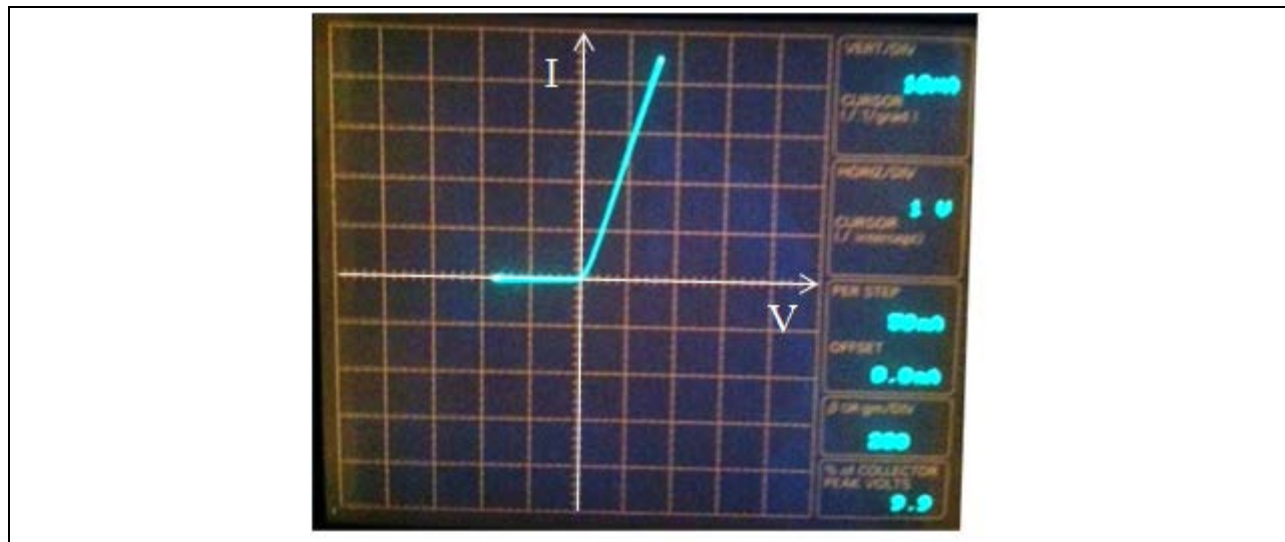

Figure 8: Current-voltage characteristic of p-type Ge on n-type Si

The need for n^+ doping on both sides of the Si-Ge junction for ohmic behavior next logically leads to the choice of a n^+-p germanium junction for the germanium photodiode as illustrated in Figure 9. The built-in voltage for this junction at room temperature will be:

$$V_{bi} = \frac{kT}{q} \ln\left(\frac{N_A N_D}{n_i^2}\right) = \ln\left(\frac{(1x10^{16})(2x10^{19})}{(2x10^{13})^2}\right) = 0.52V \tag{7}$$

where kT/q is the thermal voltage, N_A=p, N_D=n^+, and n_i is the intrinsic carrier concentration. The depletion region, where electron-hole pair absorption leads to the photogenerated current, will exist primarily on the p side of the junction with total width given by

$$\begin{aligned} W &= \sqrt{\frac{2\varepsilon(V_{bi} - V_A)}{q} \frac{1}{N_A}} \\ &= \sqrt{\frac{2(16x8.85x10^{-14}\,F/cm)(0.52V)}{1.6x10^{-19}\,C} \frac{1}{1x10^{16}/cm^3}} \\ &= 3.0x10^{-5}\,cm = 0.30\,\mu m \end{aligned} \tag{8}$$

The width of the depletion region in the n+ region is merely

$$x_n = \frac{x_p N_A}{N_D} = \frac{(0.30\mu m)(1x10^{16})}{(2x10^{19})} = 0.15nm \tag{9}$$
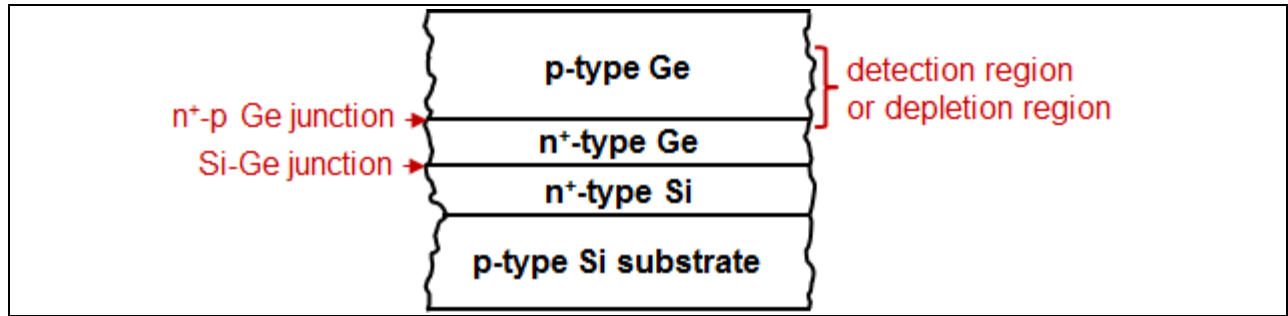
Figure 9: Germanium photodiode on a Si substrate

Either phosphorous or arsenic, common dopants in Ge, may be used as the n^+-type dopant. Activated doping concentrations of about $2x10^{19}/cm^3$ as shown in Figure 10 should be a reasonable design goal. [12] After thermal activation, a thick film of Ge would next be deposited over the ion-implanted layer which is expected to have a p-type doping concentration of about N_A=~$10^{16}/cm^3$ due to native defects that result from the lattice mismatch between the silicon substrate and the thick germanium. [2]

Figure 10: Activated conduction-band electron concentrations (n) in Ge after implantation and annealing [12]

4.0 FABRICATION
4.1 Germanium Deposition
High quality germanium growth on silicon is challenging due to a large lattice mismatch (~4%), but during the past decade, a number of researchers have demonstrated useful germanium films by electron-beam evaporation, chemical-vapor deposition, pulsed-laser deposition, and molecular beam epitaxy. We have exclusively utilized e-beam evaporation and pulsed laser deposition because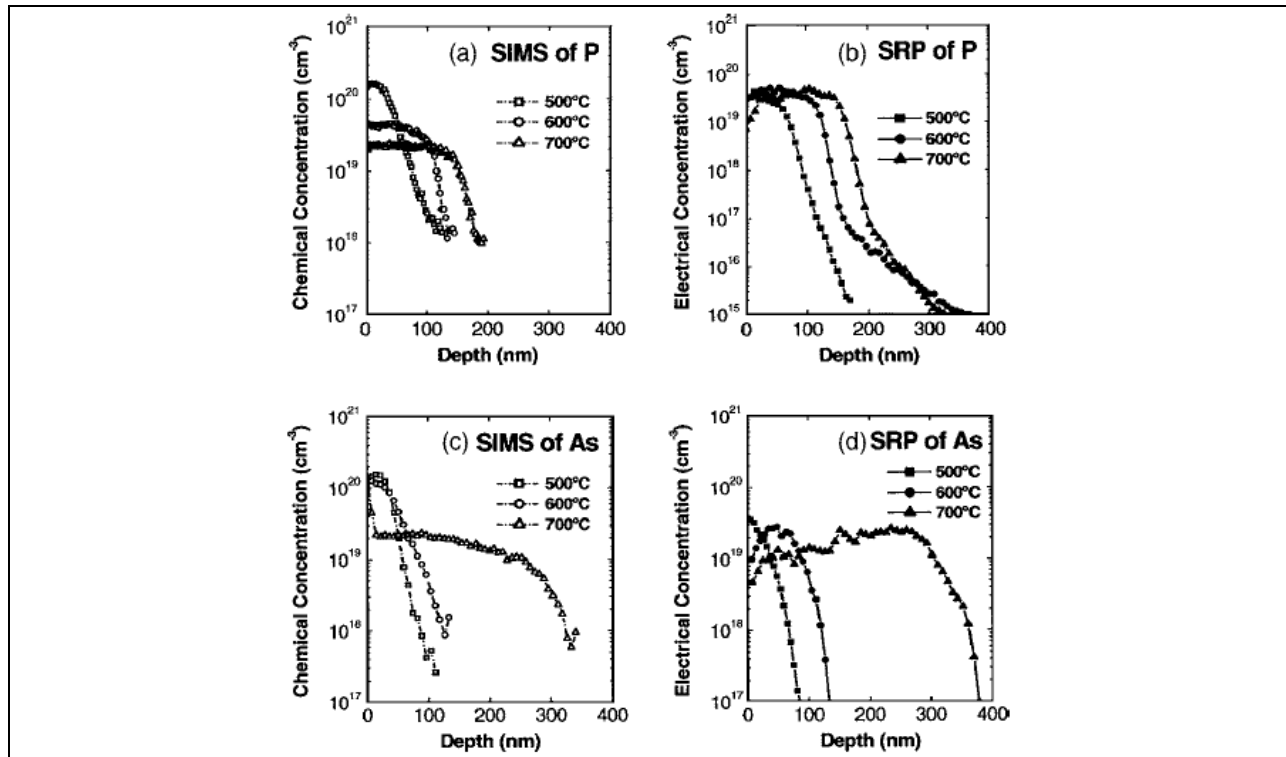 these two techniques provide us sources of both high quality amorphous germanium and textured polycrystalline germanium, respectively. Figure 11 shows the relatively flat two-theta diffraction pattern of our e-beam deposited amorphous film that contrasts with the very sharp lines of the pulsed-laser deposited (PLD) films that are indicative of a textured film.
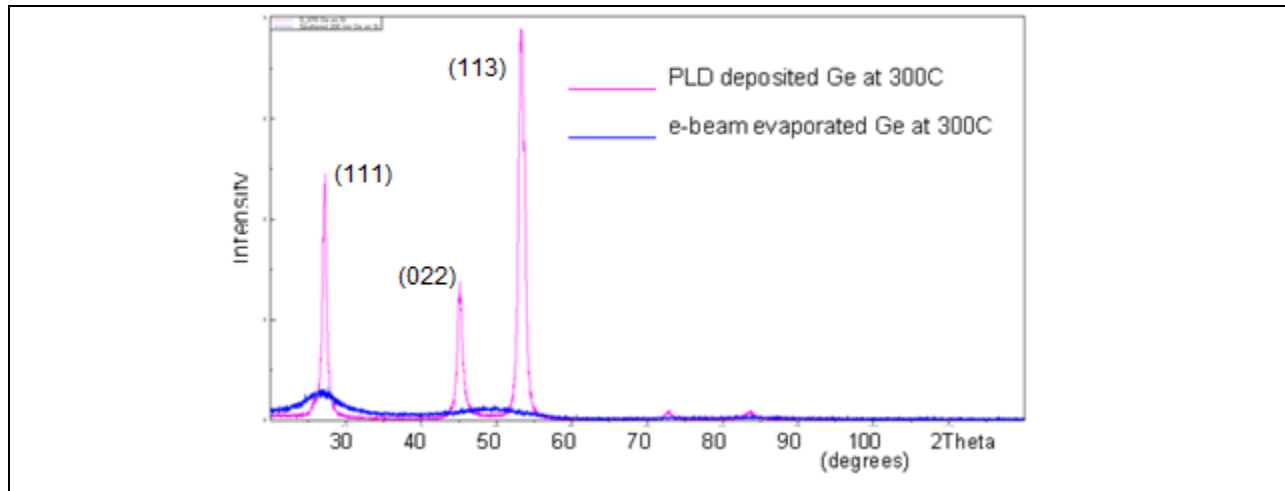

Figure 11. X-ray diffraction spectra comparing Ge films formed by electron-beam deposition and pulsed laser deposition at 300 C.

The degree of crystallinity of our films can be controlled primarily by substrate temperature and deposition technique. Lower temperature growth generally produces amorphous films. In addition, PLD will produce films with much higher levels of crystallinity than possible with e-beam deposition, probably due to the fact that Ge atoms arriving on the surface are more energetic. Like prior researchers, we have also observed that native defects associated with the lattice mismatch act as acceptors, and the doping concentration is dependent upon deposition conditions. The native doping can be directly utilized in device design, or it can be eliminated by compensation. Other researchers have also utilized surfactants during growth [13], but we have not yet explored this possibility.

4.2 Selective Etching of Germanium
The ability to realize patterned thin films is critical to the fabrication of detector structures that are compatible with various IPC designs. Although dry etch techniques and shadow masking during deposition are important, a low-cost wet etch process offers several advantages including more tolerant etch times. Yet, we are not aware of any reports in the technical literature on patterned etching by wet processes although germanium etchants such as hydrogen peroxide (H_2O_2) and chromium etchant CR-7 that react minimally or not at all with the underlying silicon are described in the literature. [14] We have observed undercutting with some of these etchants, often on the order of 7-to-1 for lateral versus vertical etching, and at times, it is clearly due to

Approved for public release; distribution unlimited

photoresist liftoff as illustrated in Figure 12. However, undercutting can be significantly reduced. Therefore, we prepared a test photoresist mask based upon the Standard Air Force Resolution Target shown in Figure 13, and we completed a comparison of various etchants for amorphous films overlaid with a Shipley 1813 positive resist pattern. Table 1 lists our results Similar experiments on textured polycrystalline films are presently being performed. It was found that hydrogen peroxide (H_2O_2) at or below room temperature (20 C) produced the sharpest patterns in the Ge films. Higher temperature H_2O_2 (50 C) resulted in significant lateral etching under the photoresist, a characteristic that could be useful for fabricating gradual tapers in the Ge thickness. Etching in chromium etchant CR-7 [15], CEP-200 [16], and RCA SC1 (a solution of NH_4OH, H_2O_2, and H_2O) resulted in etching aspect ratios between these extremes for H_2O_2. In general, room temperature or cooled etch solutions are preferred since elevated temperatures interfere with the interfacial bonding between the surface and the OH groups of the phenolic polymer base of positive photoresists. Additives to the etchant solutions may also better protect the bonding.

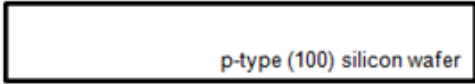**Figure 12. Micrograph of the Ge surface after selective etching in heated H_2O_2.**

Figure 13. Test photolithographic mask.
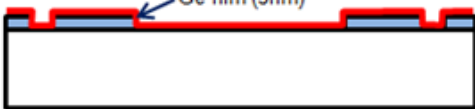
Table 1: Experimental results for selective wet etching of Ge by various solutions of Ge on Si overlaid with a Shipley 1813 positive resist pattern

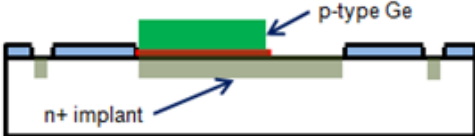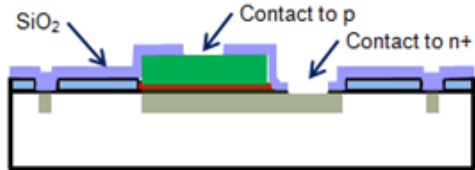| Etchant	Vertical Etch Rate	Lateral Etch Rate	Aspect Ratio
CR-7 (5C)	50 nm/min	~0.3 um/min	6 : 1
CR-7 (20C)	525nm/min	~1.3 um/min	2.5 : 1
50% CR-7 and H2O	260 nm/min	~1 um/min	4 : 1
20% CR-7 and H2O	120 nm/min	~0.6 um/min	5 : 1
20% CR-7 (w/ HMDS)	90 nm/min	~1.1 um/min	12 : 1
CEP-200 (20C)	325 nm/min	~1.6 um/min	5 : 1
30% H2O2 (5C)	20 nm/min	< 0.02 um/min	< 1 : 1
30% H2O2 (20C)	28 nm/min	~0.02 um/min	~1 : 1
30% H2O2 (50C)	64 nm/min	~2.8 um/min	45 : 1
RCA SC1	257 nm/min	~0.75 um/min	3 : 1

4.3   Photodetector

The fabrication schedule for the Ge-on-Si photodiode discussed in section 3.2 was devised and is described in Table 2. The design was next translated into the standard graphics software for producing photolithographic masks, L-Edit. This was performed for detector area sizes of 25x25, 50x50, 100x100, 200x200, and 400x400 um^2. These are shown in Figure 14. In addition, several test structures illustrated in Figure 15 were also laid out for incorporation into the masks. These will enable characterization of the doped and undoped Si and the Ge film. They include several Kelvin resistor designs, a Van Der Pauw design, and several Hall effect structures.

Table 2. Semiconductor fabrication schedule.

Semiconductor Fabrication Schedule: Ge-on-Si Photodiode

Cross-sectional Views

1. RCA wafer cleaning
   p-type (100) silicon wafer

   p-type (100) silicon wafer

2. Thermal Oxidation: 1100C, 1hour, dry, 0.1μm thickness

   SiO₂

3. Photolithography and Etch of Detector Region and Alignment Marks

   alignment mark   window for detector

4. RCA wafer cleaning

5. Germanium Deposition: 5nm Thickness
   Pulsed Laser Deposition
   or E-Beam Evaporation

   Ge film (5nm)

6. Ion Implantation of n-type dopant
   Phosphorous or Arsenic
   $N_D \sim 2 \times 10^{19}/cm^3$

   n+ implant

7. Capping Oxide over Doped Ge/Si:
   Sputtering of SiO_2

8. Thermal Annealing

9. Stripping Oxide in HF
   Both Si and Ge are impervious to HF

10. Germanium Deposition
    Thickness ~ 800nm
    Native defects provide $N_A \sim 10^{16}/cm^3$

11. Photolithography to Mask Ge Detector Region

    p-type Ge
    n+ implant

12. Etching of Ge
    ~50% H_2O_2 in H_2O at 20C

13. Protective Oxide Deposition: Sputtering of SiO_2

    SiO₂   Contact to p   Contact to n+

14. Photolithography for Contact Windows

15. Aluminum Deposition

    Aluminum

16. Photolithography to Define Aluminum Contacts and Bonding Pads
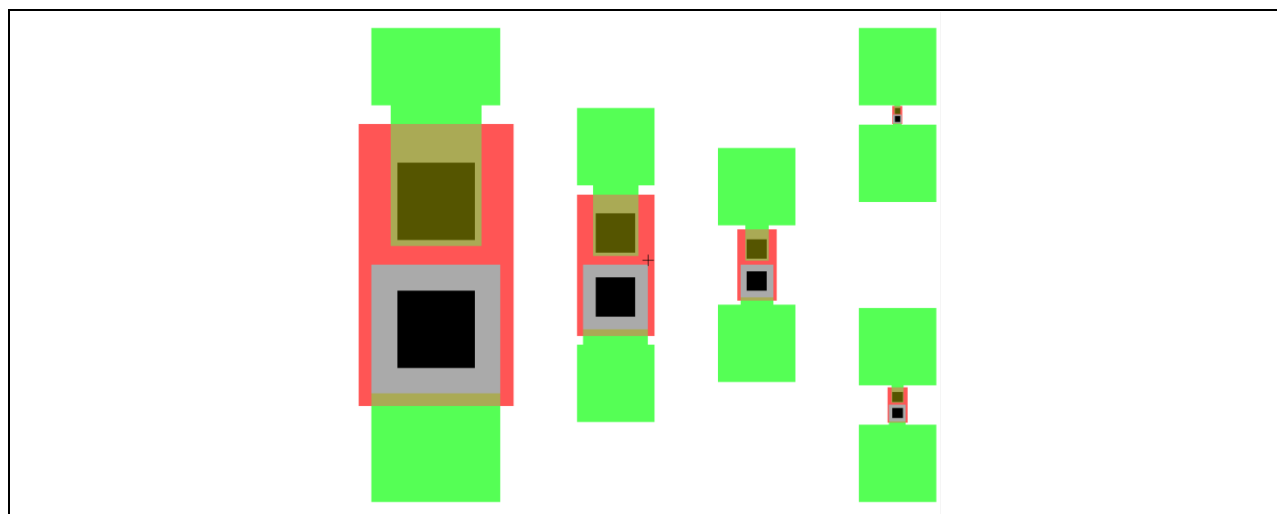
17. Aluminum Etching

18. Sintering

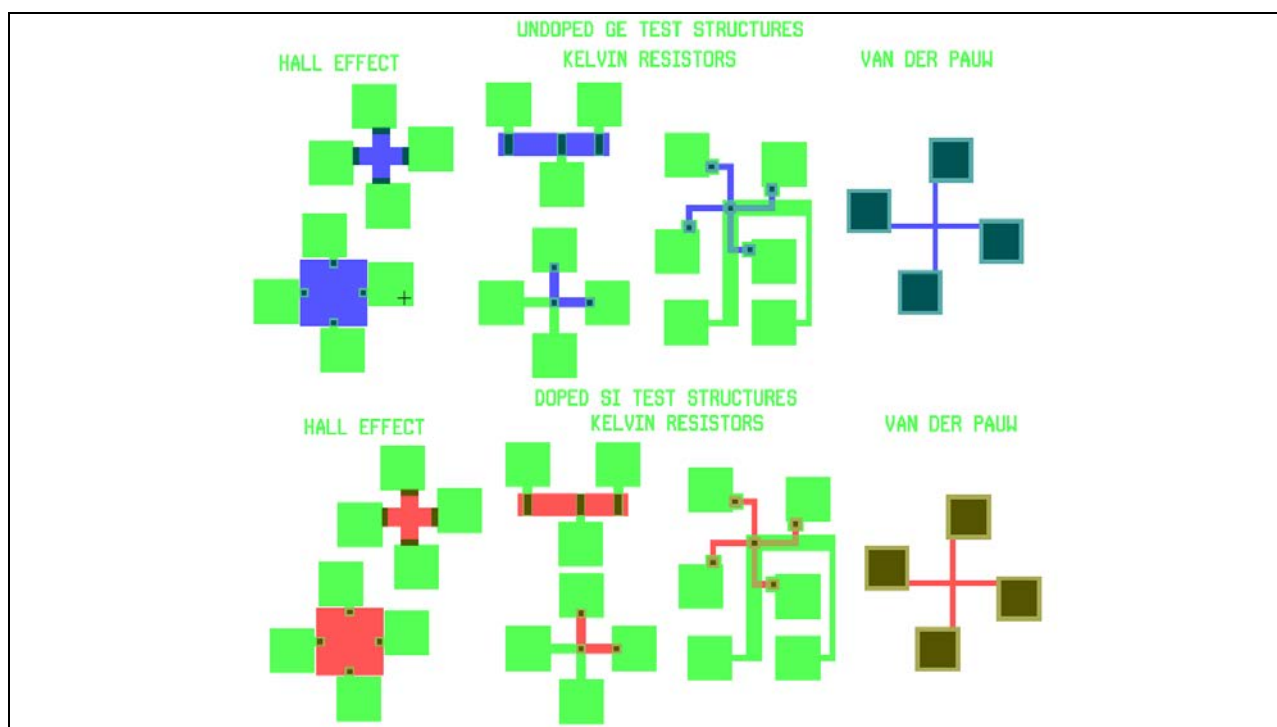**Figure 14. Plots from L-Edit files for Ge-on-Si photodetector**

Figure 15. Semiconductor test structures

5.0   CONCLUSION

In summary, germanium-on-silicon is a promising technology for enabling an integrated photonic circuit utilizing optical heterodyne detection for driving an antenna element of a phased array. Our study concluded that a photodetector is the preferred approach over utilizing a second-order nonlinear optical waveguide for heterodyne detection. We then proceeded to design a photodetector, and then began studying the processes for fabricating it. Also, we discovered that information for one of the critical processing steps, selective etching of Ge on Si, is not available in the world's technical literature. After a comparative study of processes, we concluded that either room temperature or cooled hydrogen peroxide was the optimum selective etchant.

We have also concluded that Ge-on-Si technology has specific advantages that are fundamental to nearly all integrated photonic circuits. [17] Its direct energy bandgap, slightly larger than Ge's indirect bandgap, permits band-to-band recombination/generation at an energy that corresponds to light near the optical communications wavelength of 1.55 µm, which could enable a host of IPC subcomponents including photodetectors, laser diodes, and enhanced silicon modulators. In addition, such germanium devices can be simply and inexpensively incorporated into a silicon manufacturing process.

Approved for public release; distribution unlimited

6.0 REFERENCES

1. Schuetz, C.A., R.D. Martin, E.E. Dillon, S. Shi, & D.W. Prather, "Optical Techniques for Multifunctional Millimeter-Wave Imaging Receivers," IEEE Photonics Conf (PHO) 823-824 (2011)

2. Nahata, A. and T.F. Heinz, "Generation of subpicosecond electrical pulses by optical rectification," *Optics Letters* **23**, 867-869 (1998).

3. Baehr-Jones, T., M. Hochberg, G. Wang, R. Lawson, Y. Liao, P.A. Sullivan, L. Dalton, A.K.-Y. Jen, & A. Scherer, "Optical modulation and detection in slotted Silicon waveguides," *OPTICS EXPRESS* **13,** 5216 (11 July 2005).

4. Baehr-Jones, T., J. Witzens, & M. Hochberg, "Theoretical Study of Optical Rectification at Radio Frequencies in a Slot Waveguide," *IEEE Journal of Quantum Electronics* **46,** 1634 (11 Nov 2010).

5. Duan, N. et al., "310GHz gain-bandwidth product Ge/Si avalanche photodetector for 1550nm light detection," Opt. Express 20, 11031–11036 (2012).

6. Chen, L., C.R. Doerr, L. Buhl, Y. Baeyens, and R.A. Aroca, "Monolithically integrated 40-wavelength demultiplexer and photodetector array on silicon," IEEE Photonic Tech. L. 23, 869-871 (2011).

7. Oh, J., S.K. Banerjee, and J.C. Campbell, "Metal-Germanium-Metal Photodetectors on Heteroepitaxial Ge-on-Si With Amorphous Ge Schottky Barrier Enhancement Layers," IEEE Photonics Tech. L. 16, 581-583 (2004).

8. Wietler, T.F., A. Ott, E. Bugiel, K.R. Hofmann, "Advances in surfactant-mediated growth of germanium on silicon: high-quality p-type Ge films on Si," Mat. Sci. in Semicon. Proc. 8, 73 (2005).

9. Williams, K.R., K. Gupta, and M. Wasilik, "Etch Rates for Micromachining Processing—Part II" J. Microelectromech. S. 12, 761 (Dec 2003).

10. http://www.cyantek.com/chrome-etchants.php (30 May 2013).

11. http://www.microchrometechnology.com/products_hardsurface.php (30 May 2013).

12. Chui, C.O., L. Kulig, J. Moran, W. Tsai, and K.C. Saraswat, "Germanium *n*-type shallow junction activation dependences," *Applied Physics Letters* **87**, 091909 (2005)

13. Wietler, T.F., A. Ott, E. Bugiel, K.R. Hofmann, "Advances in surfactant-mediated growth of germanium on silicon: high-quality p-type Ge films on Si," Mat. Sci. in Semicon. Proc. 8, 73 (2005)

14. Williams, K.R., K. Gupta, and M. Wasilik, "Etch Rates for Micromachining Processing—Part II" J. Microelectromech. S. 12, 761 (Dec 2003)

15. http://www.cyantek.com/chrome-etchants.php (30 May 2013)

16. http://www.microchrometechnology.com/products_hardsurface.php (30 May 2013)

17. Hopkins, F. K., K. M. Walsh, A. Benken, J. Jones, K. Averett, D. Diggs, L.-S. Tan, S. Mou, and J.G. Grote, "Germanium on silicon to enable integrated photonic circuits," **Proc. SPIE 8876**, 8876–30 (2013)

Approved for public release; distribution unlimited

LIST OF ACRONYMS, ABBREVIATIONS, AND SYMBOLS

Acronym	Definition
EO	Electro-Optic
IPC	Integrated Photonic Circuit
RF	Radio Frequency
Ge	Germanium
Si	Silicon
PLD	Pulsed-Laser Deposition
H_2O_2	Hydrogen Peroxide